Lawrence Berkeley National Laboratory
Climate & Ecosystems

Title
Wellhead based time domain reflectometry for casing integrity investigation

Permalink
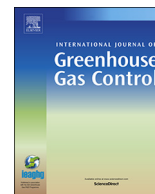https://escholarship.org/uc/item/5j88r302

Authors
Wang, Jiannan
Wu, Yuxin

Publication Date
2020-05-01

DOI
10.1016/j.ijggc.2020.103002

Peer reviewed

Wellhead based time domain reflectometry for casing integrity investigation

Jiannan Wang*, Yuxin Wu

Lawrence Berkeley National Laboratory, 1 Cyclotron Road, Berkeley, CA 94720, United States

ARTICLE INFO

ABSTRACT

Wellbore integrity is one of the most critical factors for CO_2 storage, subsurface resource extraction, and waste disposal. Wellbore integrity monitoring is challenging due to the general inaccessibility and high cost of well-logging operation in complex subsurface conditions. In this study, we tested a novel non-invasive approach for wellbore-integrity assessment based on time-domain reflectometry (TDR) method. With this method, a high-frequency electromagnetic pulse is sent into the borehole casing, and the reflected signals due to integrity-related impedance anomalies are recorded at the wellhead, providing rapid borehole integrity diagnosis without downhole deployment. Laboratory, numerical, and field experiments were conducted to prove the feasibility of this approach. The laboratory experiments with coaxial cable, resembling the typical wellbore, showed clear reflected signals from both of the damaged section and the end of the cable. Numerical sensitivity tests indicated that the TDR response is affected by the changes of the material in the borehole, including infilled fluids. Our field trial was conducted on an oil well (with a depth of 240 m) in the central valley region of southern California. The TDR records showed a clear reflection that matched both the calculated two-way travel time from the bottom of the borehole, as well as the numerical simulation. Our results suggested the feasibility of the TDR method for quick assessment of wellbore integrity based on wellhead only deployment.

1. Introduction

Wellbore integrity is of paramount importance to subsurface resource extraction, energy storage, and waste disposal. After installation, the casing and cement are subject to mechanical stress due to near-well pressure changes and fluid-induced corrosion (Wilt et al., 2018). By 2017, there are more than 900,000 active oil and gas wells (Meko and Karklis, 2017) and 3,660,940 abandoned oil and gas wells (EPA report, 2018) in the United States. A previous study suggested a significant fraction of the recently completed wells in Pennsylvania is leaking (Ingraffea et al., 2014), and this is likely true for more than one million wells in the U.S.

For steam-injection, geothermal, and Carbon Capture & Sequestration (CCS) wells, borehole corrosion is exacerbated due to the high temperature or CO_2 contained water in the wells. The impaired wellbores could result in reduced productivity, early abandonment and even leakage (*e.g.,* CO_2, methane, and other hydrocarbons) that can cause significant damages to both human and the environment, as witnessed during the recent Aliso Canyon gas leakage events (Conley et al., 2016). In addition, the vital aspect to public and regulatory acceptance of CO_2 storage is the assurance of no leak from the injection formation into the overlying potable groundwater (Keating et al., 2011;

Li et al., 2018). The co-existence of the abandoned oil and gas wells with good geological storage sites could lead to potential leakage along with these existing wells (Celia et al., 2011). Therefore, effective wellbore integrity monitoring is critical for assessing the borehole state of health, identifying damaged zone, and providing guidance for remedial actions.

The complexity of geology, geochemistry, and geomechanical conditions in the subsurface brings great challenges to wellbore integrity monitoring. Current technologies have been mostly downhole logging methods, such as wireline based ultrasonic logging (Johns et al., 2009, 2011), fiber optics sensing (Schultz et al., 2002; Cannon et al., 2013; Boone et al., 2014), electromagnetic sensing (Hawkes and Gardner, 2013), and mechanical approach (Carey et al., 2010; Carey, 2013). While these tools can provide high-resolution information of borehole conditions, they are intrusive regarding borehole occupancy and interruption to the normal operation of the wells. Besides, the downhole measurements are relatively expensive to collect. As a result, the currently available wellbore monitoring methods can only be performed infrequently, in most cases, after problems within the wells have already occurred. Moreover, for horizontal wells and high-temperature geothermal wells, the existing methods are even more challenging to deploy. These limitations render the downhole wireline tools incapable

---

* Corresponding author.
E-mail addresses: jiannanwang@lbl.gov (J. Wang), ywu3@lbl.gov (Y. Wu).

of providing enough data for better prediction of the borehole degradation trajectory, which can help provide early warning of potential borehole failures (Wilt et al., 2018).

A new generation of advanced borehole monitoring method with the following advantages is desirable: First, it should be non-intrusive, which does not require behind-casing or in-casing sensor installation or deployment, thus minimizing the potential risk of introducing new leakage pathways or interrupting the operation of the wells. Second, the new method should be cost-effective, which allows frequent monitoring of the well during its life cycle to help understand degradation trajectory and provide early warning of potential failure. Third, the new method should be operated fast, which facilitates the assessment of a considerable number of wells in a short period of time.

To address these new challenges, we tested the application of the electrical time-domain reflectometry (TDR) method for wellbore-integrity assessment. Our goal is to apply the TDR method at the wellhead without introducing downhole sensors that would require shutting down the production of the wells. Compared to the previous intrusive methods, this technique significantly reduces the operation cost and increases operation efficiency. The results presented here are focused on proofing the concept of this method. We tested our method with laboratory experiments, numerical modeling, as well as field experiments.

2. Theoretical background

Time-domain reflectometry has been used for locating faults on conductive cables or pipelines (Furse et al., 2009; Amir et al., 2010) as well as for measuring soil water content and bulk soil electrical conductivity (Topp and Davis, 1985; Herkelrath et al., 1991; Heimovaara, 1993) by sending a high-frequency electromagnetic pulses into the medium under investigation and recording the reflected signals. Similar to seismic guided waves (Wang et al., 2016), TDR signals propagate inside the conductive medium, which is under examination, and reflect at the interfaces with impedance changes (such as joints, faults, terminations). The travel time and the waveforms of the reflections (*e.g.*, shape, polarity, and magnitude) relate to the distances and the dielectric characteristics of the faults (*e.g.*, the size of the damage), respectively. Similar to reflection seismic method, the voltage reflection coefficient (R) in TDR method is defined as (Iskander, 2013):

$$R = \frac{V_r}{V_i} = \frac{Z_L - Z_0}{Z_L + Z_0},$$

(1)

where V_r is the amplitude of the reflected voltage, V_i is the amplitude of the incident voltage, Z_0 is the characteristic impedance of the cable, Z_L is the impedance of the load on the cable. As such, when the cable is completely broken, then $Z_L = \infty$, resulting in the reflection coefficient being 1. On the other hand, when there is no load, then $Z_L = 0$, the resulting reflection coefficient equals -1. For most of the characteristic impedance changes on the conductive cables, the voltage reflection coefficient is between -1 and 1.

For wellbore-integrity assessment, borehole casing can be considered as the analogy of a conductive cable, with damages treated as loads. By sending an electric pulse and collecting the reflections at the wellhead, we can analyze the characteristic impedance changes along the wave-propagation path that are indicators of potential integrity issues of the wellbore. Since the electromagnetic waves travel along the casing, we can potentially apply this TDR method to deviated or horizontal wells.

Numerical simulations are useful for sensitivity test and theoretical analysis. However, due to the thin thickness of typical casing (about 1 cm) and the long length of wellbore (from a few hundred meters to kilometers), numerical simulation of wellbore with regular grid often results in a massive amount of meshes, and is extremely computationally costly (Tang et al., 2015; Patzer et al., 2017). Because TDR waves travel primarily along the casing in 1-D mode, simulating the

electromagnetic wave in 3-D space is not necessary. In addition, the geometry of borehole casing can be considered as cylindrical symmetric. Therefore, the computation cost can be significantly reduced.

We implemented a two-step numerical modeling scheme developed by Lundquist et al. (2013): First, the 2-D cross-section of the wellbore is built based on characteristic impedance properties of different components and their functions and boundary conditions in terms of impacts on electrical voltage (V) distribution. Then, the characteristic impedance of each type of the cross-sections is calculated with the finite difference method (FDM) following the procedure developed by Kowalski (2009) and Lundquist et al. (2013). At last, all the calculated characteristic impedances are incorporated into the 1-D longitudinal modeling to simulate the overall time-domain reflectometry (TDR) response.

To calculate the characteristic impedance of the 2-D cross-section, following the implementation procedure developed by Lundquist et al. (2013), the Voltage potential (*V*) of the cross-section can be calculated by solving the Poisson equation with FD method:

$$\nabla \cdot (\varepsilon_r \nabla V) = -\frac{\rho}{\varepsilon_0},$$

(2)

where *V* is the unknown voltage potential, ρ is the charge density function, ε_r is the relative permittivity function, and ε_0 is the relative permittivity of the free-space.

With the voltage potential field been solved, the electric field potential can be found with $\boldsymbol{E} = -\nabla V$. Finally, the total charge q per unit length along the inner conductor can be determined with Gauss's law (Lundquist et al., 2013):

$$q = \varepsilon_0 \oint_S \varepsilon_r(x, y) \boldsymbol{E}(x, y) \cdot d\boldsymbol{n},$$

(3)

where $\boldsymbol{E}$ is the electric field. The closed surface can be in any shape, as long as it encloses the inner conductor while is still inside the outer metallic shield. In this study, we used the cubic square as the closed surface. After q is found, the capacitance C per unit length can be calculated (Iskander, 1992; Lundquist et al., 2013):

$$C = \frac{q}{V_0},$$

(4)

where V_0 is the excitation voltage. This value is arbitrarily defined as a boundary condition and can be fixed at a normalized value as 1.0 V.

Finally, the characteristic impedance (per unit length) of the cross-section can be calculated by utilizing the following relations (Iskander, 1992; Lundquist et al., 2013):

$$Z = \sqrt{\frac{L}{C}},$$

(5)

where C is the capacitance per unit length. L is the inductance per unit length. It is challenging to measure the inductance directly. On the other hand, the velocity of the electromagnetic wave (v_p) can be written as (Iskander, 1992):

$$v_p = \frac{1}{\sqrt{LC}},$$

(6)

If there is no dielectric insulation between the inner conductor and the outer metallic shield, we know that $v_p = v_0$ (v_0 is the speed of light in the vacuum), then:

$$v_0 = \frac{1}{\sqrt{LC_0}},$$

(7)

where C_0 is the capacitance per unit length in the absence of any dielectric media and can be calculated by simulating an identical system as Eq. (4), but without any embedded insulation.

Substituting Eqs. (6) and (7) into Eq. (5), we have the formula to calculate the characteristic impedance (per unit length) of the cross-section:
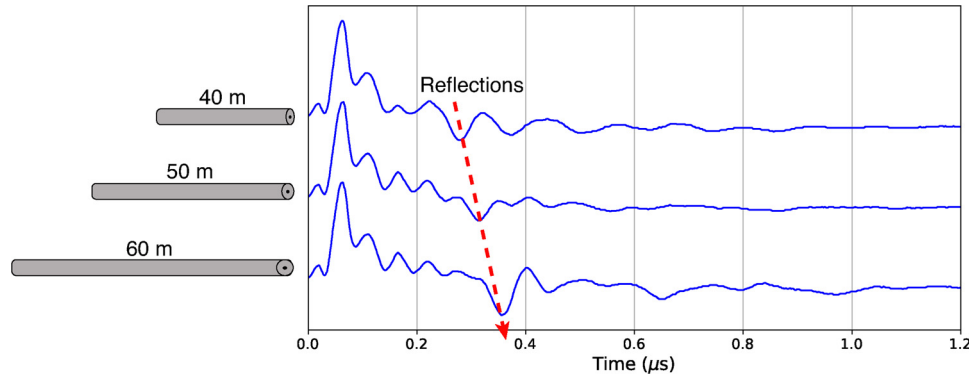
Fig. 1. TDR measurements of the ASTM-B-3 110-copper wires with lengths of 40 m, 50 m, and 60 m. The red dashed arrow indicates the reflections from the end of the wires.

$$Z = \sqrt{\frac{L}{C}} = \sqrt{\frac{LC_0}{CC_0}} = \frac{1}{v_0\sqrt{CC_0}}, \tag{8}$$

3. Laboratory experiments and numerical modeling scheme

Laboratory experiment under simplified, ideal condition is useful to understand the essential signal characteristics of the TDR waves along the conductors. Fig. 1 shows a preliminary test example of the TDR responses from three copper wires (ASTM-B-3 110) with no load. Three cables with different lengths were tested: 40 m, 50 m, and 60 m. The naked wire was laid out on the ground mainly contacting the air, with a few places touching the ground. The velocity factor of the wire is about 90 (electromagnetic wave travels at about 90% of the speed of light in vacuum). Due to the impedance contrast between the reflectometer (Megger Teleflex VX) and the wire (*i.e.*, the loading stage), reflections were observed at the beginning of each trace for all wires. Since there was no load on the cable ($Z_L = 0$), negative polarizing returns were expected and can be observed at the end of the traces from all three wires (indicated by the red-dashed arrow in Fig. 1). As is shown in Fig. 1, the two-way travel times of the negative-polarizing reflections increase proportionally with the length of the wires. The calculated travel distances, with the velocity factor of the wire, from these reflections match with the lengths of the wires. The visible ambient noise after the loading stage is likely due to various reasons, such as the distortions on the wire, the ambient electromagnetic interference, and the contact with the ground.

Further experiments were conducted using coaxial cable (RG-58/U). The comparison between the experimental results and the numerical simulations were performed. As is shown in Fig. 2a, the coaxial cable has a layered but simplified structure compared to the two-casing wellbore, with two conductors separated by a dielectric material. Hence, we use the coaxial cable as the simplified analogy of a wellbore with two casings. The inner core and the metallic jacket can be used as an analogy of the production tubing and the conductor casing, respectively. The dielectric insulation and the outmost PVC shield can be considered as the cement or oil mud used to complete the wells. The relative permittivity of dielectric insolation (ε_{di}) and the outmost PVC (ε_{pvc}) is 2.25 and 3.18, respectively. The dimensions of the model are shown in Table 1. Because all the electrical properties of the RG-58/U coaxial cable are well known, we can use the coaxial cable as the reference benchmark to check the numerical model described above. In the laboratory experiment, we used an 80-m long R-58/U coaxial cable, which has the velocity factor of 65.9 (Coaxial Cable Specifications, 2019) (propagates at 65.9% of the speed of light in vacuum) and a linear Q factor of 38.4 dB per 100 m.

The numerical modeling scheme described previously was tested on the coaxial cable (RG-58/U) with known dielectric properties of each component and can be treated as homogeneous along the length of the cable (Fig. 2a). Fig. 2b shows the numerical model of the cross-section of the RG-58/U coaxial cable. The dimensions and the dielectric properties are the same as mentioned above. Fig. 2c shows the voltage potential field of the RG-58/U coaxial cable. As we expected, each of the components presented in the model is homogeneous and spatially continuous, and most of the energy is confined inside the metallic shield. Following the procedure from Eq. (2)-(8), the calculated characteristic impedance is 50.7590 Ω, which is close to the actual value, 50 Ω, indicating the reliability of this numerical modeling procedure.

Similarly, we calculated the characteristic impedance of the damaged cable in order to simulate the TDR response from the broken section on the cable. Fig. 2d shows the cross-section of the coaxial cable with a 120° cutaway. The frequency we used in the simulation was 2 GHz. Fig. 2e shows the voltage potential field of the damaged coaxial cable. Comparing the simulated voltage potential field of the intact cable to the damaged cable, we can see that, when the cable is intact (Fig. 2c), the gradient of the potential field radiates away from the center conductor through the dielectric material with no gradient inside the central conductor in any directions. Also, because the outer metallic shield of the cable was set as a perfect conductor, thus no current leak-off is observed on the simulated cross-section. On the other hand, when the cable was partially cut off (Fig. 2d), while the majority of the current is still propagating along the inner conductor, the voltage potential radiation pattern presented in the model is heterogeneous and spatially directional toward the damaged area (Fig. 2e). Without the perfect insulation, we can see that the current leaks away from the central conductor through the cutaway.

To simulate the overall TDR response along the cable, we assembled the characteristic impedance of the intact and the damaged sections of the cable into the 1-D model. Same as the experiment setting, the cutaway was modeled as in the middle of the cable (40 m mark) of the 80-m cable. The input signal has a voltage of 40 V and a pulse width of 20 ns. These simulation results were compared with laboratory experiments that are shown in Fig. 3a and b. The blue curves represent the TDR response of the intact 80-m long coaxial cable, whereas the red curves are the TDR response of the same cable damaged in the middle at 40 m.

The impedance contrast at the junction between the reflectometer and the coaxial cable is responsible for the small reflected waveform observed at the beginning of the TDR traces for both damaged and intact cables. When the cable is intact (the blue line), we can see one reflection at around 0.75–1 μs and a slightly weaker one at around 1.75–2 μs. Because the cable is intact, meaning the characteristic impedance of the load $Z_L = 0$, we should receive a reflection with the negative polarity from the end of the cable, according to Eq. (1). Considering the velocity factor of the coaxial cable is 65.9, the first reflection with negative polarity is from the end of the cable (indicated by the blue arrow in Fig. 3a). At the time about twice of the two-way travel time of the first reflection, we can see another negative-polarity
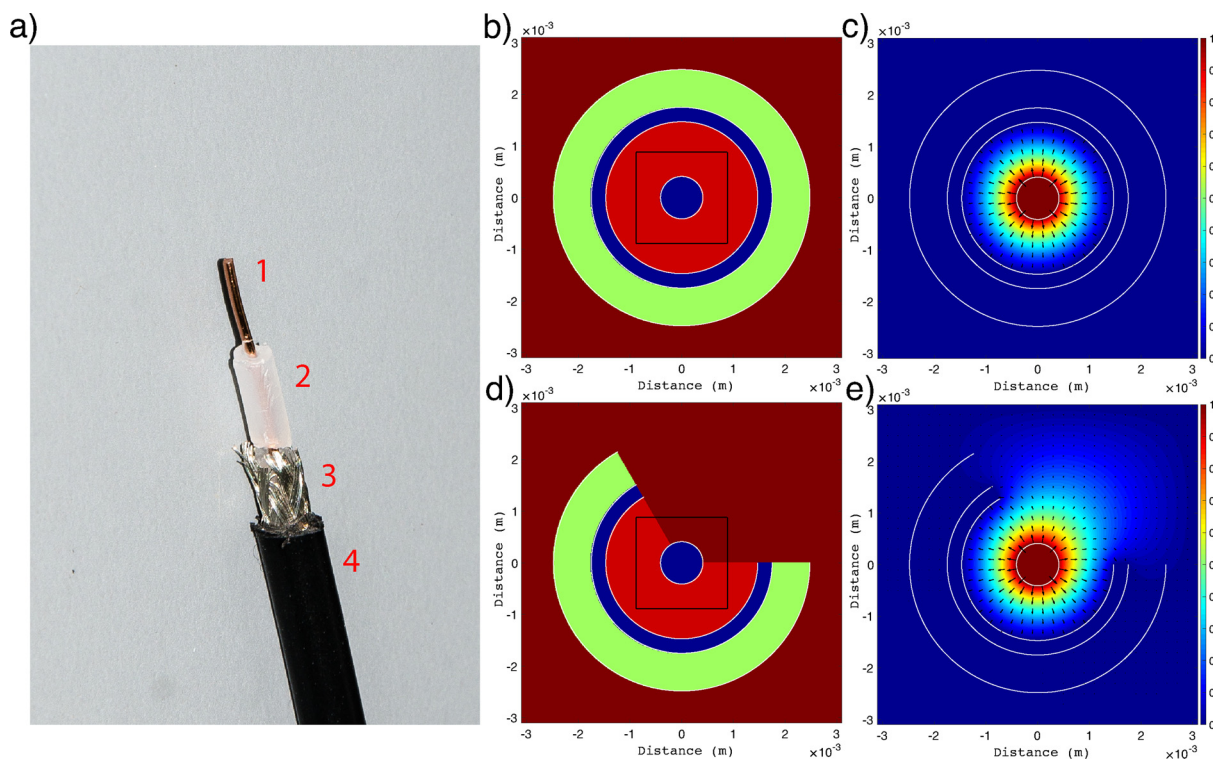
Fig. 2. Cross-section of the numerical modeling of RG-58 coaxial cable. (a) The coaxial cable cutaway. 1 is the copper core. 2 is the inner dielectric insulator. 3 is the metallic shield. 4 is the outer PVC. (b) The numerical model of the intact coaxial cable according to the dimensions shown in Table 1. The light green is the outmost PVC shield. The blue represents the inner conductor and metal jacket. The red is the dielectric insulation layer. The black box in the middle is the contour for the Gauss's integration in Eq. (3). (c) Normalized voltage potential field. The black arrows represent the electric field directions. (d) The numerical model of the damaged coaxial cable with 120° cutaway. (e) Normalized voltage potential field. The black arrows represent the electric field directions.

Table 1
RG-58/U coaxial cable dimensions.

Layer	Inner diameter (mm)
Inner core	0.84
Dielectric insulation	2.94
Metal jacket	3.14
PVC	4.96

wavelet with weaker amplitude, at around 1.75 μs. We interpret this reflection as the first multiple. When the cable is damaged with 120° cutaway, the calculated characteristic impedance of the damaged section is 56.1546 Ω. From the TDR response (the red curve in Fig. 3a), we observe a strong reflection with positive polarity at around 0.4–0.6 μs, about half of the two-way travel time from the end of the intact cable (indicated by the blue arrow in Fig. 3a). Also, the estimated two-way travel time of this reflection matches the location of the damaged section. Comparing with the reflection from the undamaged cable (indicated by the blue arrow in Fig. 3a), we can see it has the almost identical waveform but a weaker amplitude and opposite polarity. We interpret this first reflection as due to the damage in the middle of the cable. At 0.75–1 μs, the same two-way travel time from the end of the intact cable, we see another much weaker reflection with positive but more complicated waveform. We suggest this is the overlap of both reflections from the end of the cable, which has the negative polarity, and the first multiples of the reflections from the cutaway, which as the positive polarity. Also, the damaged cable has stronger attenuation. As a result, no further multiple can be seen after the end of the cable (1 μs).

Fig. 3b shows the numerical simulation of the TDR response of both the intact (the blue curve) and the 120° cutaway (the red curve) coaxial cable. We used the impulse waveform as the source waveform and added 2% white noise to the modeling results. Comparing Fig. 3a and

Fig. 3b, the experiment results match with the modeling results well, indicating the numerical simulation scheme of the TDR is reliable. Because of the structural similarity between the coaxial cable and the two-casing wellbore, these TDR measurements on the coaxial cable suggest the feasibility of the TDR method for subsurface borehole applications, yet multiple complicating factors, such as geological heterogeneity, infrastructure noise, and imperfect casing sealing present significant challenges which will be discussed in the field test section later.

4. Numerical sensitivity test

The laboratory experiments indicate the feasibility of the TDR application on the well-integrity assessment and the reliability of the numerical models for simulating borehole responses. Here, we utilize the numerical code to explore the sensitivity of the method to different damage patterns under various application scenarios. As is shown in the previous sections, the characteristic impedance of the medium determines the TDR response. In the case of the subsurface wellbores, the characteristic impedance can be affected by multiple factors, such as the structure of the wells, the status of the casing, and the fluid inside the wells. The numerical experiments in Fig. 2 indicate the integrity of the wellbore affects the characteristic impedance a lot. In addition to the casing itself, the fluid inside the casing may have an impact on the TDR response as well. For oil/CO_2 wells, the crude oil and CO_2 only has a relative permittivity around 2.2 (Friisø et al., 1998; Vralstad et al., 2009) and 1.5 (Moriyoshi et al., 1993), respectively. But for geothermal wells, the hot water (100 °C) has the relative permittivity of 80 (Archer and Wang, 1990). Analyzing the sensitivity of the characteristic impedance to these factors is necessary for wellbore integrity assessment.

In this section, we analyze the effect on the characteristic impedance from wellbore damage while hosting different types of fluids
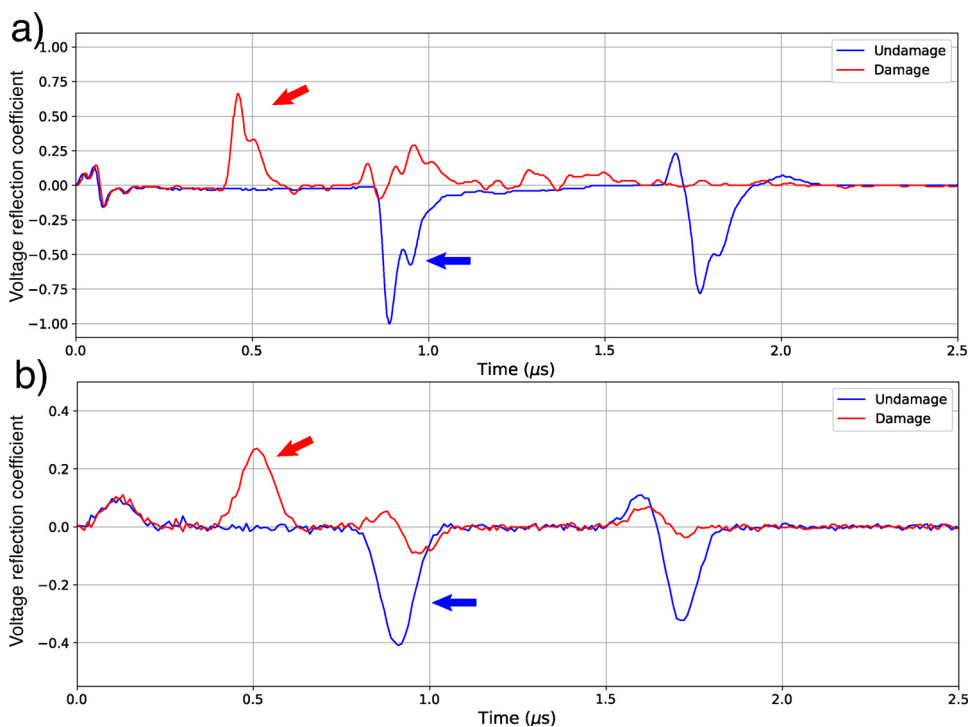
Fig. 3. Comparison between the numerical simulation and the laboratory experiment of the TDR response from coaxial cable. (a) Laboratory experiment of the TDR response. (b) Numerical modeling of the TDR response. The red curves are the results from the damaged coaxial cable, whereas the blue curves are from the intact cable. The red arrows in the plots indicate the TDR reflections from the end of the cable. The blue arrows indicate the TDR reflection from the damaged part of the cable.
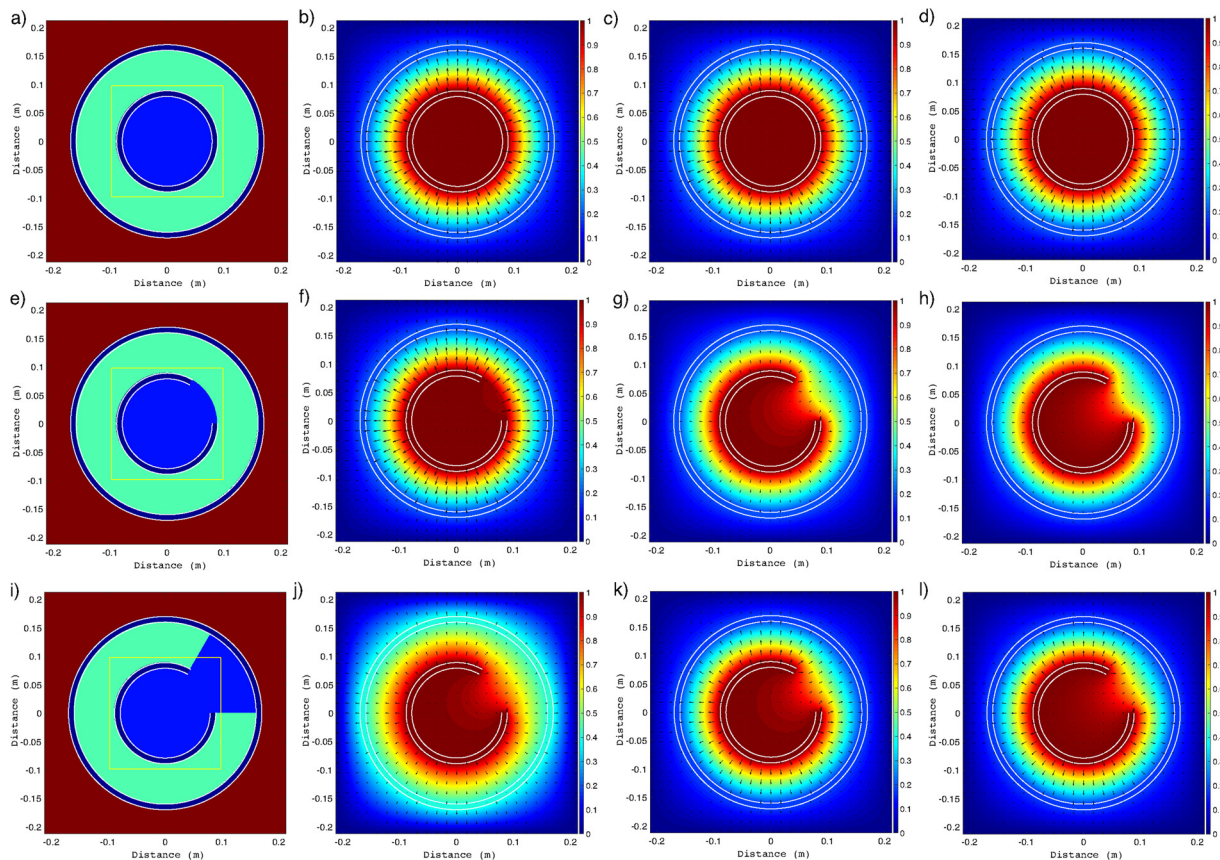
Fig. 4. 2-D numerical modeling of the wellbore. (a) The model of the intact wellbore. Dark blue rings are the casings. Light blue is the fluid inside the well. Cyan is the cement formation. The yellow box in the middle is the contour for the Gauss integration in Eq. (3). (b)–(d) Normalized voltage potential field when the fluid inside the well is hot water, crude oil, and CO_2, respectively. The black arrows represent electric field direction. (e) The model of the damaged wellbore. Only the casing is damaged by the 60° cutaway. (f)–(h) Normalized voltage potential field when the fluid inside the well is hot water, crude oil, and CO_2, respectively. (i) The model of the damaged wellbore with 60° cutaway. The cement is intruded by the wellbore fluid. (j)–(l) Normalized voltage potential field when the fluid inside the well is hot water, crude oil, and CO_2, respectively.
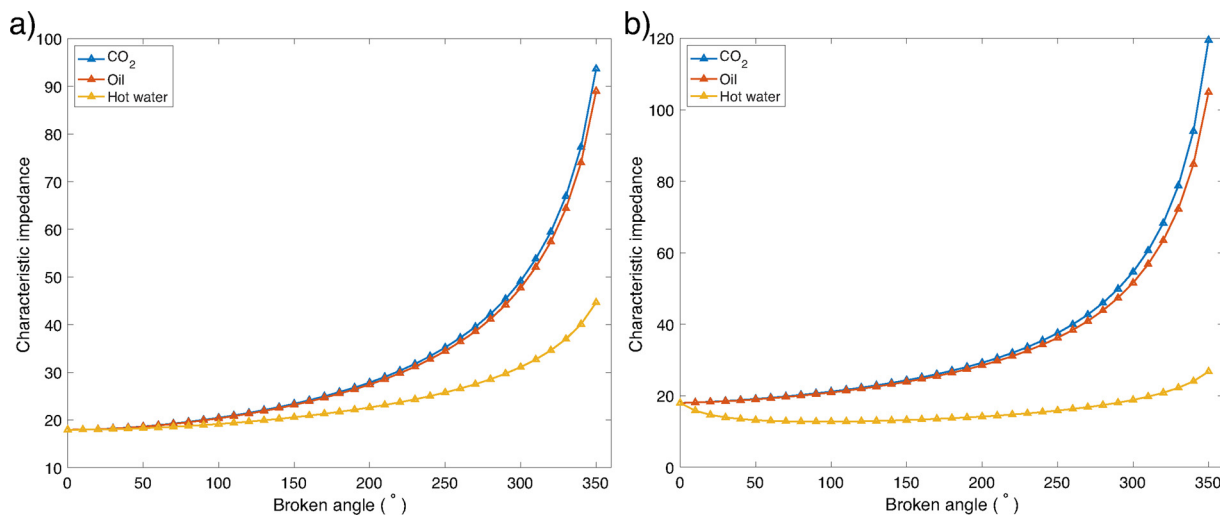
Fig. 5. Characteristic impedance vs. Wellbore damage size. The size of the damage is represented by the angle of the cutaway. The color of the curves represents the wellbore fluid. Blue: CO_2. Orange: crude oil. Yellow: hot water. (a) The cement is intact. (b) The cement is intruded by the wellbore fluid.

(i.e., oil, CO_2, or water) inside the well. We implemented the numerical simulation schemes illustrated from Eq. (2)–(8). For simplicity, we only analyzed the simplest scenario: the model with only two casings. Same as most of the surface and production casings in the industry, in this model, the casings, with the thickness of 10 mm, were set to have the outer diameters of 340 mm and 178 mm, respectively. Cement, with the relative permittivity of 5 (Robert, 1998; Kharkovsky et al., 2002), was filled between the casings. The background geologic formation around the wellbore was set to have the same relative permittivity of dolomite ($\varepsilon_r = 10$) (Davis and Annan, 1989; Daniels, 1996; Martinez and Brynes, 2001). Three scenarios were simulated in this test: (1) the wellbore was intact, (2) only the inner casing was damaged, and (3) both the inner casing and the intermedium cement was damaged. For each scenario, we simulated both oil well and geothermal wells (filled with hot water). The frequency we used in the simulation was 2 GHz. The closed surfaces used for calculating the characteristic impedance (in Eq. (3)) are indicated by the yellow boxes in Fig. 4a, e, and i. For both of the damaged casing scenarios, the damages were modeled as 60° cutaway (Fig. 4e, i).

Fig. 4a shows the cross-section of the intact well. The current was applied to the inner casing. The simulated normalized voltage potential fields are shown in Fig. 4b (geothermal well), Fig. 4c (oil well), and Fig. 4d (CO_2 well). The voltage potential field from both types of the wells are similar to the coaxial cable (Fig. 2c). The gradient of the potential field radiates away from the center conductor in the dielectric material with no gradient inside the central conductor in any directions. The voltage potential field of the model is cylindrically homogeneous, and the majority of the energy is confined inside the wellbore. However, since the outer casing is not a perfect conductor as the metallic shield of the coaxial cable, we can see the current leaks into the surrounding geological formation (Fig. 4b, c). Due to higher relative permittivity of the hot water (Fig. 4b), the geothermal well has larger current leakage than oil and CO_2 well (Fig. 4c, d).

When only the inner casing is damaged, the fluid will fill the void caused by the damaged casing (Fig. 4e). The simulated normalized voltage potential fields are shown in Fig. 4f (geothermal well), Fig. 4g (oil well), and Fig. 4h (CO_2 well). Due to the damage on the casing, the model becomes cylindrically heterogeneous: The dielectric medium replaces part of the metallic medium. As we can see from Fig. 4f–h, the low-potential field "flows" into the inner casing through the gap on the casing as the fluid replaced the metallic casing. Comparing the voltage potential field of the geothermal well (Fig. 4f) with the oil/CO_2 well (Fig. 4g, h), the potential field of the geothermal well has much less directional voltage leakage than the oil/CO_2 well. This is because the hot water ($\varepsilon_r = 80$) is much more conductive than the crude oil

($\varepsilon_r = 2.2$) and CO_2 ($\varepsilon_r = 1.5$). After the hot water replaces the metallic casing, the alteration of the conductivity is not as much as the case of the oil/CO_2 well. Thus, the oil/CO_2 well has less current leak-off into the surrounding geological formation than the geothermal well.

When both the inner casing and the cement are damaged, the wellbore fluid will intrude into the cement between casings (Fig. 4i). The simulated normalized voltage potential fields are shown in Fig. 4j (geothermal well), Fig. 4k (oil well), and Fig. 4l (CO_2 well). Same as the scenario which only the casing is damaged, we can see the directional voltage leakage for geothermal well (Fig. 4j), oil well (Fig. 4k), and CO_2 (Fig. 4l). However, different from the second scenario (Fig. 4f–h), the geothermal well (Fig. 4j) shows a significantly greater current leakage than the oil/CO_2 well (Fig. 4k, l). Also, comparing Fig. 4f and j, we can see, if the cement of geothermal well is also broken, significant more current leaks from the inner casing to the cement. Due to the intrusion of the fluid, not only the conductive casing, but the cement (dielectric medium) is also partially altered by the fluid. Therefore, when the high-conductive hot water flows into the cement, a large amount of electrical current leak into the cement, causing a greater increase of the potential field in cement (Fig. 4j). On the contrary, for oil/CO_2 well (comparing Fig. 4g, h and k, l), because the cement ($\varepsilon_r = 5$) is then replaced with less conductive crude oil ($\varepsilon_r = 2.2$) or CO_2 ($\varepsilon_r = 1.5$), the current leakage is reduced with the broken cement. Since the relative permittivity difference between the cement and the oil/CO_2 is not significant, as a result, the voltage potential field is not very different between the scenario 2 (Fig. 4g, h) and 3 (Fig. 4k, l).

As discussed above, the return signals for TDR measurements are directly affected by the characteristic impedance of the wellbore. Therefore, analyzing how the state of the wellbore integrity affects the characteristic impedance is essential for wellbore-integrity assessment. Here, we investigate how the size of the damage, as well as the wellbore fluid, affect the characteristic impedance of the wellbore. For the scenarios discussed above with oil, CO_2, and geothermal wells, the characteristic impedance is calculated by following the scheme developed by Lundquist et al. (2013) from Eq. (2)–(8). Fig. 5 shows the change of the characteristic impedance regarding the size of the wellbore damage, the wellbore fluid, and the state of the cement between casings. When only the steel casing is damaged (Fig. 5a), regardless of the type of wellbore fluid, the characteristic impedance of the wellbore is mainly affected by the size of the damage, i.e., the loss of the conductive casing. As a result, the characteristic impedance increases as the damage size increases. Because crude oil and CO_2 are less conductive, compared to the hot water, the characteristic impedance of oil/CO_2 well increases faster than the geothermal well. Therefore, while the characteristic

impedance of geothermal, CO_2, and oil well are sensitive to the size of the damage on the casing, the characteristic impedance of the oil/CO_2 well is more sensitive to damage when compared to the geothermal well.

For the cases that both casing and cement are damaged, the correlation between the characteristic impedance and the size of the cutaway on the wellbore is shown in Fig. 5b. The characteristic impedance of the oil and CO_2 wells (blue and orange curves in Fig. 5b, respectively) is very similar to the scenario when only the casing is damaged (blue and orange curves in Fig. 5a, respectively). As is discussed before, this is because the difference of the relative permittivity between the crude oil/CO_2 and the cement is not significant. Therefore, when the oil/CO_2 is replacing the cement, the characteristic impedance is not affected much. On the other hand, for the geothermal well, when the hot water intrudes into the cement (shown as the yellow curve in Fig. 5b), we can see the characteristic impedance decreases at first, followed by a small, gradual increase. The characteristic impedance changes in a small range (less than $10\,\Omega$ per unit length), indicating that the characteristic impedance of the geothermal wellbore is not sensitive to the size of the damage if the cement is also damaged. We interpret this is because when the damage is small, the loss of the metallic casing has a significant impact, resulting in an increase of the characteristic impedance at first. As the size of the damage increases, the influence of the highly-conductive hot water replacing the low-conductive cement becomes more significant, resulting in the overall conductivity of the dielectric section (between two casings) increases. Considering the voltage potential of the cross-section that is shown in Fig. 4h, even though the casing loses 1/6 of its metallic material, the dielectric medium between casings become more conductive. When the size of the wellbore damage is small, the conductivity increase of the dielectric section, due to the hot water intrusion, overcomes the conductivity decrease, due to the loss of the metallic casing. As the size of the damage becomes more significant, the effect of losing the steel casing starts to surpass the effect of replacing the cement with the hot water. Due to the two opposing processes, which are replacing metallic casing with highly-conductive hot water and replacing low-conductive cement with highly-conductive hot water, the characteristic impedance of the geothermal well is not sensitive to the size of the damage.

For monitoring and early warning of the slow chronic leakage on the casing, detecting the thinning of the borehole because of the corrosion until the breakthrough of the fluid is also crucial. In addition to the sensitivity test in Fig. 5, we also investigate how thinning of the casing and the size of the damage affect the characteristic impedance of the wellbore. Similar to the sensitivity test in Fig. 5, different infilled wellbore fluids, $i.e.$, hot water, crude oil, and CO_2, are simulated. The results are shown in Fig. 6. The thinning of the casing is represented by the corrosion percentile of the thickness. For all three types of infilled fluids, characteristic impedance increase as the size of the cutaway on the wellbore. As is shown in Fig. 6, the characteristic impedance is

much more sensitive to the size of the damage when the casing is broken through. In our numerical test, the breakage point in order to be detected is 50° cutaway. However, if the casing is not entirely broken through, the breakage point in order to be detected is around 120° for the oil/CO_2 well (Fig. 6b, c) and around 220° for the geothermal well (Fig. 6a). Similar to the previous numerical tests (Figs. 4 and 5), the conductivity of the infilled fluid has a high impact on the characteristic impedance change when the infilled fluid replaces the metallic casing due to the corrosion. In addition, the characteristic impedance of the wellbore gets a significant boost when the casing is broken through for all types of the wellbore infilled fluid.

In reality, the damage in the wellbore may partially cut into the cement. For the oil/ CO_2 well, the characteristic impedance is sensitive to the size of the damage. For geothermal well, the sensitivity of the characteristic impedance to the damage size is situational: If only the shallow part of the cement is damaged, the characteristic impedance is sensitive, but less sensitive than the oil/CO_2 well, to the size of the damage. If damage cuts deeply into the cement, it is difficult to infer the state of the damage from the characteristic impedance of the wellbore.

5. Field experiment

To test the TDR method in realistic field condition, we conducted measurements at an oilfield in the Central Valley region of southern California. Note that while these are oil wells, the bottom temperature of the wells is roughly at 260 °C due to the long term steam injection. Therefore, the condition of the well can also be used as the analogy of geothermal wells. Fig. 7a shows the diagram of the measured well, which is undamaged and is about 240 m (800 ft) deep with multiple casing strings. Fig. 7b shows the photography of the wellhead. Even though the well is currently not in production and used as the observation well, we could not open the wellhead and access the individual casings inside. We applied the TDR measurement (Megger Teleflex VX) directly on the wellhead without opening the well. The input pulse had a voltage of 70 V and a frequency of 4500 kHz. Because the wellhead is closed, we did not have access to each individual casings. In order to receive the return signal, we connected the TDR receiver to an adjacent unconnected well (50 m away).

Similar to the laboratory experiments, we first simulated the voltage potential of the cross-section, the characteristic impedance, and the TDR response. Fig. 8a shows the numerical model of the wellbore cross-section. The dimensions of the model are shown in Table 2. The dielectric medium between the casings is cement ($\varepsilon_r = 5$). The background geological formation is dolomite ($\varepsilon_r = 10$). As is discussed in the sensitivity test, for non-broken well, the fluid in the wellbore does not affect the characteristic impedance. So, for simplicity, we assume the well is uniformly filled with crude oil ($\varepsilon_r = 2.2$).

After implementing Eq. (2) and $\boldsymbol{E} = -\nabla V$, we calculate the normalized voltage potential of the cross-section (Fig. 8b) as well as the
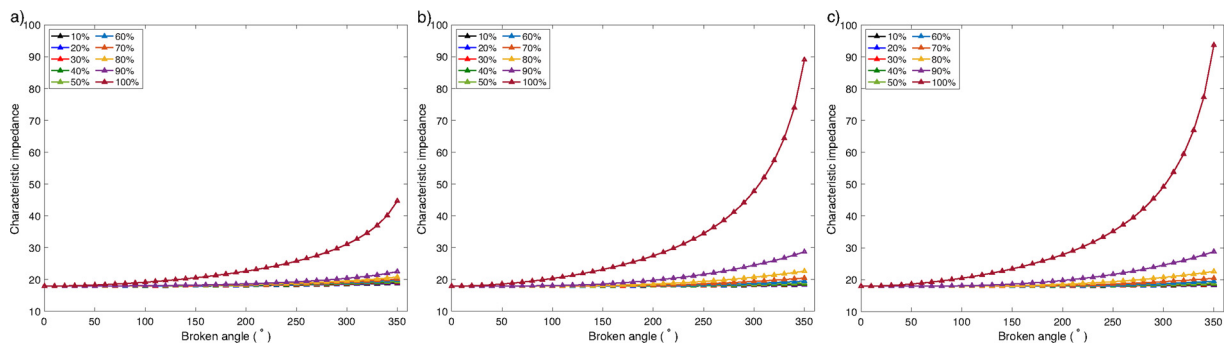

Fig. 6. Characteristic impedance vs. Wellbore damage size at different corrosion percentile. The cement is intact. The size of the damage is represented by the angle of the cutaway. The corrosion percentiles are represented by different color-coded curves. (a) The wellbore-infilled fluid is hot water. (b) The wellbore-infilled fluid is crude oil. (c) The wellbore-infilled fluid is CO_2.
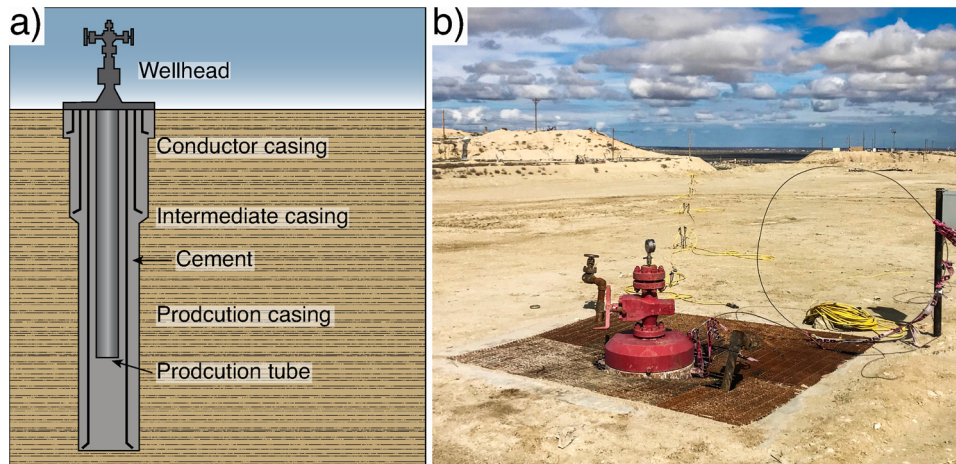
Fig. 7. The observation well measured in the oilfield in the Central Valley region of southern California. (a) Schematic diagram of the observation well. (b) The photograph of the actual wellhead.

electric potential (Fig. 8c), respectively. The numerical result is similar to the ones of the laboratory experiment in Fig. 4b. Both the voltage and electrical potential field indicates that, though most of the energy is constrained inside wellbore, there are still current leaking into the surrounding geological formation. Since the casings are not the perfect conductor, unlike the laboratory experiment (Fig. 4b), more electrical energy radiates into the surrounding medium (Fig. 8b, c).

Based on the 2-D cross-section model, we calculated the characteristic impedance per unit length of the wellbore and incorporate the result into the 1-D simulation of the TDR response. The yellow box in Fig. 8a is the closed surface used in the Gauss integration (Eq. (3)). The source frequency we used in the 1-D simulation was set as 4500 kHz, the same as the frequency we used in the field measurement. Because the well is not broken, we expect only to receive a reflection from the bottom of the well. Knowing the bottom of the production tube is at the depth of 237.7 m (780 ft.), and the velocity factor of the tube is 80–90, the two-way travel time of the bottom reflection should be 1.76–1.98 μs. The numerical modeling of the TDR response is shown in Fig. 9a. As is shown in the simulated TDR response, except the loading-stage reflection at the very beginning of the signal trace, we can see a reflection at the time 1.6–1.8 μs, matching with the direct calculation of the travel time.

Fig. 9b shows the TDR response from the field test. At the time of 0–0.25 μs, we can see the loading-stage reflection. At the time of 1.8–2 μs, another distinctive reflection can be easily identified. Given the velocity factor of the tube at 80–90, this reflection calculated to be

Table 2
Dimensions of the oil well in the California central valley oilfield.

Casing	Inner diameter (mm)	Outer diameter (mm)	Length (mm)
Production tube	75.9968	88.9	197.7
Production casing	226.5934	244.475	231.6
Intermediate casing	320.421	339.725	167.6
Conductor casing	436.8038	457.2	28.3

from about 230–255 m (755–837 ft) deep. The reflection matches the direct calculated two-way travel time of the reflection from the bottom of the production tube and the result from the numerical simulation (Fig. 7a).

Due to the simplicity of the numerical model not taking into account of the complexity of the uncertain variables in the field test, such as inherent casing impedance variability, geological heterogeneity, the presence of conductive centralizers and imperfect cement job among others, it is expected to see that the amplitude of the bottom reflection is smaller than the numerical simulation in the simplified, perfect case. In addition, between the initial loading stage and the bottom reflection, we can see the ringing reflections with almost linearly decreasing amplitude. These reflections are likely the result of these complex factors presented in the wellbore, such as the centralizers between casings, cement imperfection, and the variable interference with surrounding geological formations. Nevertheless, these smaller features may contain
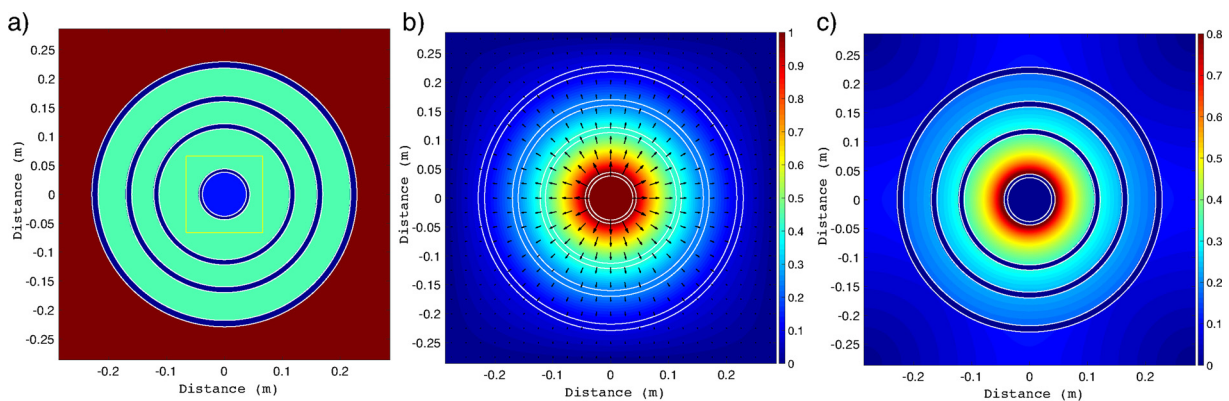

Fig. 8. The 2-D numerical simulation of the observation well in Fig. 7. (a) The cross-section of the numerical model. The dark blue rings represent the casings. Light blue represents the crude oil inside the well. Cyan represents the cement formation between casings. The yellow box in the middle is the contour for the Gauss integration in Eq. (3). (b) Normalized voltage potential field. The black arrows represent electric field direction (c) Normalized electric potential field calculated from $E = -\nabla V$.
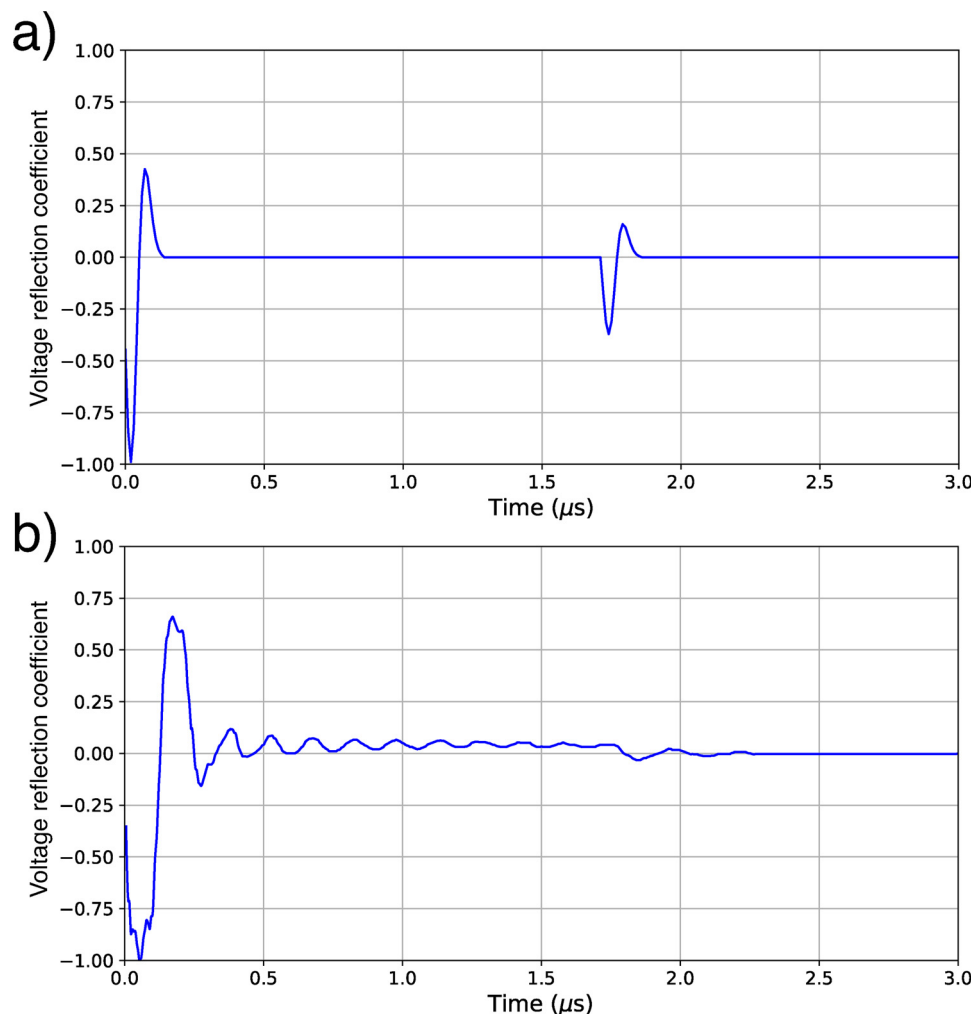
Fig. 9. TDR pulse responses from the 1-D numerical modeling and the field experiment at the observation well. (a) Numerical simulation result of the TDR response. (b) TDR response of the field test at the oilfield.

useful information regarding the finer scale information of the boreholes, yet direct validation and confirmation are challenging at field scales, and additional laboratory tests are required. Additional tests on three more abandoned wells yield similar results were not shown in this paper. These field test results demonstrate for the first time the applicability of the TDR method for wellbore integrity assessment in deep, complicated boreholes.

6. Discussions

The TDR method is essentially a method of detecting the characteristic-impedance changes of the propagated medium. For borehole applications, it is under the assumption of the 1-D characteristic impedance model along a conductive waveguide, *i.e.*, steel casing in our case. Analyzing the correlation between the characteristic impedance and the state of integrity is the key to the wellbore integrity assessment in our study. As we can see from the numerical experiments in Figs. 4–6, the characteristic impedance is sensitive to the integrity state of the wellbore that is related to the degree of damage, the depth of the corrosion, as well as the type of fluids present inside the wellbore. Specially, for geothermal wells, the hot water inside the casing has high relative permittivity ($\varepsilon_r = 80$). Therefore, when the hot water is only replacing a small portion of the inner casing, the change of the relative permittivity distribution is not significant. As a result, the voltage potential difference between the intact well (Fig. 4b) and the broken well with only 60° damage on the inner casing (Fig. 4f) is small. As the

damage on the casing increases, more conductor (the casing) is replaced by the less conductive fluid (the hot water), resulting in a large increase of the characteristic impedance of the cross-section as shown in Fig. 5a. Therefore, for geothermal well with casing-only damage, the TDR method could be used as an integrity diagnosis tool. In the scenario when the hot water is not only invading the casing, but also the cement, the loss of the conductor (the casing) is partially compensated by the alternation of the cement ($\varepsilon_r = 5$) with the hot water ($\varepsilon_r = 80$), resulting in an overall smaller increase, or even decrease, of the impedance. If the size of the damage is relatively small, the application of TDR method is more challenging based on these numerical results. Laboratory and field experiments for testing these simulations have not been conducted.

In the case of oil/CO_2 wells, because of the low relative permittivity ($\varepsilon_r = 2.2$ for oil, and $\varepsilon_r = 1.5$ for CO_2) of the fluid, the damaging of the wellbore and invasion of crude oil/CO_2 is a scenario of replacing the conductor (the casing) or the cement ($\varepsilon_r = 5$) with a low-permittivity dielectric material, *i.e.*, the crude oil and CO_2. In the case of casing-only damage, such a change of impedance is significant, resulting in a readily detectable signal of TDR. In the case of additional cement damage, because of the similar impedance between oil/CO_2 and cement, additional impedance change due to cement damage is small, resulting in a similar potential field distribution and impedance change when compared with the case of casing-only damage. These are illustrated in Fig. 4g and k, and the blue and orange lines in Fig. 5a and b. As a result, regardless of the integrity of the cement, we can see the positive

correlation between the cutaway on the casing and the characteristic impedance of the wellbore. Again, these numerical simulation results need to be validated via experimentations at both lab and field scales.

In addition to detecting the location of the potential damages, further information regarding the magnitude of damage is also desirable, although more challenging to acquire. Based on the sensitivity test shown in Fig. 5, we can see the curves increase relatively slow when the broken angle is less than 50°. It is especially true for the geothermal case. Therefore, the characteristic impedance is sensitive to the size of the damage, for both the oil/CO$_2$ well and the geothermal well with minimum damage in the cement. The numerical chronic corrosion test (Fig. 6) shown that the increasing rate of the characteristic impedance is relatively slow if the casing is not broken through. The breakage point in order to be detected is around 120° for the oil/CO$_2$ well (Fig. 6b, c) and around 220° for the geothermal well (Fig. 6a). When the casing is corroded through, the characteristic impedance gets significantly increased. However, these tests were based on simple numerical models. The signals from realistic conditions in practical applications with many complexing factors will most likely be dampened because of the complicate geological formation, the noise from the external magnetic field, and the extensive length of the well. Thus, it may be challenging to distinguish small differences between noisy signals. Many of these unknown factors can be eliminated in the time-lapse monitoring mode when time series analyses are conducted, e.g., the influence from the environment and the structure of the wellbore. In reality, the shape, the depth, and the number of the damages could vary instead of the singular fan-shape, the received TDR signals only indicate the combination result of the alternation of the conductive metallic casing. The non-uniqueness of the 1-D TDR measurement leads to uncertainty in inferring the exact damage condition. For example, if the loss of casing from single damage is equivalent to multiple damages combined, the resulting characteristic impedance would be the same. How these different patterns impact the impedance signal need to be analyzed further. Because the TDR method we proposed in this paper is based on the assumption of the 1-D model with assembled characteristic-impedance elements. Consequently, the TDR method is incapable of determining the directionality of the damage. Furthermore, due to the high velocity of the electromagnetic wave, the spatial resolution of the TDR method is likely low.

The field test showed the TDR response from the bottom of the casing along with other small reflective features from the earlier portion of the signal traces. Due to our limited knowledge of the wellbore structure, we are unable to determine the exact cause of these earlier ringing reflections. As we can see from the TDR record in Fig. 9b, the bottom reflection in the field test is distinguishable but relatively weak. The well we tested is only about 240 m and not damaged. How the TDR method performs on the deeper well and the damaged well is still subjects of further investigation. Most of the wells are hundreds or thousands meters, the attenuation from the casing, the surrounding formation, as well as the external magnetic field still need more investigation. Because the geological formation around the wellbores also contributes to the TDR response, studying the coupled effects on the TDR response from the geological variation along the borehole is also needed for future study. In this paper, numerical simulation is only used as the theoretical framework for sensitivity analysis and interpretation. With more detailed information about the wellbore structure and the surrounding geological environment, we can incorporate the forward numerical modeling into the inversion process iteratively. Furthermore, if the status of the wellbore is well known, we can also potentially use the TDR method as a quick surveying method to investigate the geological formation around the wellbores. The simple numerical mode we presented was not built with the capability for full scale simulation of the EM wave propagation behavior that might result in different signal patterns from different damage patterns, e.g., casing vs. cement damage. Our current model suggests that it would not tell if actual damages are on the casing or both casing and the cement. However, a more sophisticated numerical model and more elaborated lab and field tests might be able to tell the differences. As a proof of concept study, these are not included in the scope of this manuscript.

7. Conclusions

We tested a novel, non-invasive approach for diagnosing the integrity of the subsurface wellbores based on the time-domain reflectometry method. Although the TDR method has been applied in other fields, such as detecting defected cables or estimate soil moisture contents, this is the first attempt to apply such a method for wellbore integrity assessment. In order to prove the concept of this approach, we conducted a number of numerical simulations, laboratory experiments, and field experiments.

For numerical simulations, we implemented a two-step modeling scheme developed by Lundquist et al. (2013). First, we calculated the characteristic impedance of the 2-D cross-section of the wellbore using FDM. Then, we incorporated the characteristic impedance into 1-D longitudinal modeling to acquire the overall TDR response. Due to the structural similarity between the coaxial cable and two-casing wellbore, we conducted several laboratory experiments using the coaxial cable as the simplified analogy model for testing the TDR approach. In the laboratory experiments, the calculated characteristic impedance of the coaxial cable matched its real value, indicating the reliability of our numerical modeling scheme. The TDR responses in the laboratory experiments on both the intact and the damaged coaxial cables matched the numerical modeling, in terms of reflection polarity and travel time, suggesting the feasibility of applying the TDR method for wellbore integrity diagnosis.

Numerical sensitivity test indicated the characteristic impedance of the low-conductive fluid (oil/CO$_2$) well is sensitive to the size of the damage. For geothermal well, the relationship between the characteristic impedance and the damage size is situational: the characteristic impedance is only sensitive to the size of the damage when the majority of the damage is on the casing. However, it would be difficult to infer the state of the geothermal well if most of the damage is in the cement. For both low- and high- conductive fluid well, the corrosion depth also plays an important role in the characteristic impedance changes. When the casing is corroded through, the characteristic impedance is significantly more sensitive to the size of the damage. In reality, the damage in the wellbore is often the combination of irregular patchy shapes with varies damage depth. Because of the non-uniqueness of the 1-D TDR signal, it would be challenging to infer the shape, depth, and size of the damages.

We also conducted the field test in an oil field in the Central Valley of southern California. The field experiment showed clear TDR reflection from the bottom of the well, which matched the travel-time calculation from the numerical modeling. This dataset demonstrated for the first time, the feasibility of getting TDR signals from impedance changes that are relevant to potential wellbore integrity issues under realistic and complex field conditions. The measured TDR signals at the field scales were attenuated and interfered by the complicating factors of the wellbores, including geological heterogeneity, impedance variability, cement imperfection, among others. With more detailed information about the wellbores, the interpretation, and the numerical simulation of the TDR response is expected to be improved. In the future, the forward modeling of the TDR response could also be incorporated into the inversion process.

While the concept of the TDR method has been proven for the wellbore integrity assessment, numerous limitations warrant future research. Specifically, because the numerical approach applied in this research was based on the 1-D model, it cannot provide the specific shape, depth, and location of the damage on the wellbore. The influence from the geologic formation, the attenuation of the casing, and the external magnetic field needs further investigation. The large velocity and wavelength of the electromagnetic wave may limit the spatial

resolution of the method. More study on improving signal resolution and signal/noise ratio is needed in the future. Full scale simulation of the EM wave propagation behavior is also needed in the future.

Authors' contributions

Jiannan Wang: Conceptualization, Methodology, Software, Data curation, Writing – Original draft preparation, Visualization, Investigation.

Yuxin Wu: Supervision, Conceptualization, Methodology, Writing – Reviewing and Editing.

Conflicts of interest

The authors declare no conflicts of interest.

Acknowledgements

References

Amir, N., Barzelay, O., Yefet, A., Pechter, T., 2010. Condenser tube examination using acoustic pulse reflectometry. J. Eng. Gas Turbines Power 132, 014501.

Archer, D.G., Wang, P., 1990. The dielectric constant of water and debye-hückel limiting law slopes. J. Phys. Chem. Ref. Data 19, 371–411.

Boone, K., Ridge, A., Crickmore, R., Onen, D., 2014. Detecting leaks in abandoned gas wells with fiber-optic distributed acoustic sensing. IPTC 2014: International Petroleum Technology Conference.

Cannon, R.T., Aminzadeh, F., et al., 2013. Distributed acoustic sensing: state of the art. SPE Digital Energy Conference.

Carey, J.W., 2013. Geochemistry of wellbore integrity in CO2 sequestration: Portland cement-steel-brine-CO2 interactions. AGU Fall Meeting Abstracts.

Carey, J.W., Svec, R., Grigg, R., Zhang, J., Crow, W., 2010. Experimental investigation of wellbore integrity and CO2-brine flow along the casing-cement microannulus. Int. J. Greenh. Gas Control 4, 272–282.

Celia, M.A., Nordbotten, J.M., Court, B., Dobossy, M., Bachu, S., 2011. Field-scale application of a semi-analytical model for estimation of co2 and brine leakage along old wells. Int. J. Greenh. Gas Control 5, 257–269. https://doi.org/10.1016/j.ijggc.2010.10.005. http://www.sciencedirect.com/science/article/pii/S1750583610001544.

Coaxial Cable Specifications, 2019. Coaxial Cable Specifications. Available from: http://www.rfcafe.com/references/electrical/coax-chart.htm (12.07.19).

Conley, S., Franco, G., Faloona, I., Blake, D.R., Peischl, J., Ryerson, T., 2016. Methane emissions from the 2015 Aliso Canyon blowout in Los Angeles, CA. Science aaf2348.

Daniels, D., 1996. Surface-Penetrating Radar? IEE Radar, Sonar, Navigation and Avionics Series 6. The Institute of Electrical Engineers, London.

Davis, J.L., Annan, A., 1989. Ground-penetrating radar for high-resolution mapping of soil and rock stratigraphy 1. Geophys. Prospect. 37, 531–551.

EPA Report, 2018. Draft Inventory of U.S. Greenhouse Gas Emissions and Sinks: 1990–2016, EPA 430-P-18-001. U.S. Environmental Protection Agency.

Friisø, T., Schildberg, Y., Rambeau, O., Tjomsland, T., Førdedal, H., Sjøblom, J., 1998.

Complex permittivity of crude oils and solutions of heavy crude oil fractions. J. Dispers. Sci. Technol. 19, 93–126.

Furse, C., Smith, P., Diamond, M., 2009. Feasibility of reflectometry for nondestructive evaluation of prestressed concrete anchors. IEEE Sens. J. 9, 1322–1329.

Hawkes, C.D., Gardner, C., 2013. Pressure transient testing for assessment of wellbore integrity in the IEAGHG Weyburn-Midale CO2 monitoring and storage project. Int. J. Greenh. Gas Control 16, S50–S61.

Heimovaara, T., 1993. Design of triple-wire time domain reflectometry probes in practice and theory. Soil Sci. Soc. Am. J. 57, 1410–1417.

Herkelrath, W., Hamburg, S., Murphy, F., 1991. Automatic, real-time monitoring of soil moisture in a remote field area with time domain reflectometry. Water Resour. Res. 27, 857–864.

Ingraffea, A.R., Wells, M.T., Santoro, R.L., Shonkoff, S.B., 2014. Assessment and risk analysis of casing and cement impairment in oil and gas wells in Pennsylvania, 2000–2012. Proc. Natl. Acad. Sci. 111, 10955–10960.

Iskander, M.F., 1992. Electromagnetic Fields and Waves. Prentice Hall Upper Saddle River.

Iskander, M.F., 2013. Electromagnetic Fields and Waves. Waveland Press.

Johns, J.E., Aloisio, F., Mayfield, D.R., et al., 2011. Well integrity analysis in Gulf of Mexico wells using passive ultrasonic leak detection method. SPE/ICoTA Coiled Tubing & Well Intervention Conference and Exhibition.

Johns, J.E., Blount, C.G., Dethlefs, J.C., Julian, J.Y., Loveland, M.J., McConnell, M.L., Schwartz, G.L., et al., 2009. Applied ultrasonic technology in wellbore-leak detection and case histories in Alaska North Slope wells. SPE Prod. Oper. 24, 225–232.

Keating, E.H., Hakala, J.A., Viswanathan, H., Capo, R., Stewart, B., Gardiner, J., Guthrie, G., Carey, J.W., Fessenden, J., 2011. The challenge of predicting groundwater quality impacts in a co2 leakage scenario: results from field, laboratory, and modeling studies at a natural analog site in new Mexico, USA. Energy Proc. 4, 3239–3245.

Kharkovsky, S.N., Akay, M.F., Hasar, U.C., Atis, C.D., 2002. Measurement and monitoring of microwave reflection and transmission properties of cement-based specimens. IEEE Trans. Instrum. Meas. 51, 1210–1218.

Kowalski, M.E., 2009. A simple and efficient computational approach to chafed cable time-domain reflectometry signature prediction. Annual Review of Progress in Applied Computational Electromagnetics.

Li, Z., Fall, M., Ghirian, A., 2018. Ccs risk assessment: groundwater contamination caused by co2. Geosciences 8, 397.

Lundquist, E.J., Nagel, J.R., Wu, S., Jones, B., Furse, C., 2013. Advanced forward methods for complex wire fault modeling. IEEE Sens. J. 13, 1172–1179.

Martinez, A., Brynes, A.P., 2001. Modeling Dielectric-Constant Values of Geologic Materials: An Aid to Ground-Penetrating Radar Data Collection and Interpretation, vol. 247 Kansas Geological Survey Lawrence, Kansas.

Meko, T., Karklis, L., 2017. The Washington Post: The United States of Oil and Gas. https://www.washingtonpost.com/graphics/national/united-states-of-oil/.

Moriyoshi, T., Kita, T., Uosaki, Y., 1993. Static relative permittivity of carbon dioxide and nitrous oxide up to 30 mpa. Berichte der Bunsengesellschaft für physikalische Chemie 97, 589–596.

Patzer, C., Tietze, K., Ritter, O., 2017. Steel-cased wells in 3-d controlled source em modelling. Geophys. J. Int. 209, 813–826.

Robert, A., 1998. Dielectric permittivity of concrete between 50 MHz and 1 GHz and GPR measurements for building materials evaluation. J. Appl. Geophys. 40, 89–94.

Schultz, R.L., Robison, C.E., Bayh III, R.I., Stewart III, B.B., Nutley, B.G., Oag, J.G., Mahjoub, N., 2002. Method and apparatus for placing and interrogating downhole sensors, US Patent 6,408,943.

Tang, W., Li, Y., Swidinsky, A., Liu, J., 2015. Three-dimensional controlled-source electromagnetic modelling with a well casing as a grounded source: a hybrid method of moments and finite element scheme. Geophys. Prospect. 63, 1491–1507.

Topp, G., Davis, J., 1985. Time-domain reflectometry (tdr) and its application to irrigation scheduling. Advances in Irrigation, vol. 3. Elsevier, pp. 107–127.

Vralstad, H., Spets, Ø., Lesaint, C., Lundgaard, L., Sjöblom, J., 2009. Dielectric properties of crude oil components. Energy Fuels 23, 5596–5602.

Wang, J., Stewart, R.R., Dyaur, N.I., Bell, M.L., 2016. Marine guided waves: subbottom property estimation and filtering using physical modeling data. Geophysics 81, V303–V315.

Wilt, M., Um, E., Weiss, C., Vasco, D., Petrov, P., Newman, G., Wu, Y., 2018. Wellbore integrity assessment with casing-based advanced sensing. In: 43rd Workshop on Geothermal Reservoir Engineering. Stanford University.